



HAL
open science

Green Luminescence in Zero-Dimensional Lead bromide hybrid material (C₅H₉N₃)₂PbBr₆: Experimental and Theoretical Studies

Mohamed Ikbal Houchati, Hela Ferjani, Youssef Ben Smida, Abderrazek Oueslati, Nassira Chniba-Boudjada, Oscar Fabelo, Jean-François Bardeau, Werner Paulus, Monica Ceretti, Ahmed Hichem Hamzaoui

► To cite this version:

Mohamed Ikbal Houchati, Hela Ferjani, Youssef Ben Smida, Abderrazek Oueslati, Nassira Chniba-Boudjada, et al.. Green Luminescence in Zero-Dimensional Lead bromide hybrid material (C₅H₉N₃)₂PbBr₆: Experimental and Theoretical Studies. *Journal of Molecular Structure*, 2024, 1295 (Part 2), pp.136687. 10.1016/j.molstruc.2023.136687 . hal-04296545

HAL Id: hal-04296545

<https://univ-lemans.hal.science/hal-04296545v1>

Submitted on 23 Nov 2023

HAL is a multi-disciplinary open access archive for the deposit and dissemination of scientific research documents, whether they are published or not. The documents may come from teaching and research institutions in France or abroad, or from public or private research centers.

L'archive ouverte pluridisciplinaire **HAL**, est destinée au dépôt et à la diffusion de documents scientifiques de niveau recherche, publiés ou non, émanant des établissements d'enseignement et de recherche français ou étrangers, des laboratoires publics ou privés.

Green Luminescence in Zero-Dimensional Lead bromide hybrid material (C₅H₉N₃)₂PbBr₆: Experimental and Theoretical Studies

Mohamed Ikbal Houchati ^{a,b,*}, Hela Ferjani ^{c,*}, Youssef Ben Smida ^a, Abderrazek Oueslati ^d, Nassira Chniba-Boudjada ^e, Oscar Fabelo ^f, Jean-François Bardeau ^g, Werner Paulus ^b, Monica Ceretti ^b, Ahmed Hichem Hamzaoui ^a

^a *Laboratory of Valorization of Useful Material, National Centre of Research in Materials Science, University of Carthage, Technopol Borj Cedria, BP 73, Soliman 8027, Tunisia*

^b *Institut de Chimie Moléculaire et des Matériaux-UMR 5253, C2M: Chimie et Cristallochimie des Matériaux, Université de Montpellier 2, Montpellier, France*

^c *Chemistry Department, College of Science, Imam Mohammad Ibn Saud Islamic University (IMSIU), Riyadh 11623, Kingdom of Saudi Arabia*

^d *Laboratory of Spectroscopic Characterization and Optical Materials, Faculty of Sciences, University of Sfax, B.P. 1171, 3000 Sfax, Tunisia*

^e *Laboratoire de Cristallographie, CNRS, 25 Avenue des Martyrs, BP 166, Grenoble, 38042 Cedex 9, France*

^f *Institut Laue-Langevin, 71 Avenue des Martyrs, 38000, Grenoble, France*

^g *Institut des Molécules et Matériaux du Mans UMR CNRS 6283, Faculté des Sciences/Le Mans Université, Avenue Olivier Messiaen, Le Mans, 72085 Cedex 9, France*

* Corresponding author

E-mail address: hfferjani@imamu.edu.sa (H. Ferjani).

In this work, we describe the preparation of a new zero-Dimensional (0D) lead bromide hybrid material, with the structural formula (C₅H₉N₃)₂PbBr₆, of which crystallographic, thermal, optical, and electrical properties have been studied and analyzed. Single crystals of (C₅H₉N₃)₂PbBr₆ material were grown using a slow evaporation solution method at room temperature. The molecular structure reveals that the crystal packing is made of iso-lated [PbBr₆]⁴⁻ units into which organic (C₅H₉N₃)²⁺ cations are embedded and linked by a combination of N/C-H...Br hydrogen bonds and stacking interactions forming a three-dimensional network. The Hirshfeld surface analysis and fingerprint plots facilitates a quantification of non-covalent intermolecular interactions, which are crucial in building the supramolecular architectures. Upon photoexcitation, the crystals exhibit an efficient green emission band covering a large spectral region from 400 to 700 nm peaking at 592 nm. The optical band gap was calculated to be E_g = 3.45 eV. The electrical conductivity of this material shows that the most suitable equivalent circuit is represented by a single parallel cell formed by (R_g||CPE_g), the value of the activation energy is 1.18 eV. Thermal analysis reveals that the decomposition of the sample starts from 275 K. Density functional theory (DFT) was performed to determine the electronic structure of the tilted compound. The DFT calculation shows that the title compound is direct semiconductor with a band gap energy of about 2.97 eV.

1. Introduction

Organic-inorganic Hybrid materials (OIHMs) have recently received extraordinary attention from researchers due to their unique physical properties [1–5]. OIHMs constitute a new class of semiconductor materials exhibiting excellent optoelectronic properties [6], making them promising candidates for applications in photovoltaic (PV) devices and LED-type light emitting devices [7,8]. The focus of this field is mostly devoted towards 3D hybrid materials owing to the high efficiency of their solar cells. Lead perovskite MAPbI₃ (where MA= CH₃NH₃) is a representative of this kind of material. MAPbI₃ has been discovered to be

a remarkable photovoltaic material [9–11], with a conversion efficiency of 25% [12] when employed in single-junction solar cells, equivalent to commercial silicon-based solar cells. Recently, there has been an increase in interest in lower dimensional hybrids for a variety of applications [13,14]. Zero-dimensional hybrid materials have gained attention for their unique properties and potential applications in various fields, including optoelectronics, energy harvesting, and quantum computing. Unlike traditional three-dimensional materials, zero-dimensional materials have no extended crystalline structure and consist of discrete, nanoscale clusters or quantum dots of these materials. These clusters are surrounded by organic ligands or surfactants

that help stabilize the structure and prevent aggregation. One of the key advantages of zero-dimensional materials is their enhanced stability compared to their three-dimensional counterparts, which can be sensitive to moisture and heat. These hybrids are defined by a unique crystal structure in which anionic metal halide polyhedron is embedded and completely isolated by organic cations [15,16]. They exhibit tunable bandgaps and strong emission properties, making them promising candidates for use in optoelectronic devices such as light-emitting diodes and solar cells. The emission of 0D organic metal halides is induced by the radiation relaxation of local excitons due to the spatial restrictions of isolated metal halides, and typically displays efficient broadband emission with a substantial Stokes shift upon photoexcitation and high photoluminescence quantum efficiencies (PLQEs) [17–20]. Considering its distinctive properties, it is a promising candidate to be employed in solid-state lighting. The large Stokes shift causes most of the energy to be lost as vibration, which makes it challenging for 0D metal halides to emit blue light [21]. Nevertheless, low 0D hybrids with efficient blue emissions are still uncommon. Most of them have excitation peaks in the near ultraviolet (UV) region, while they emit significantly Stokes shifted spectra large Stokes shift and a wide FWHM [22,23]. As a result, achieving blue emission by decreasing Stokes shift is critical in the investigation of 0D hybrid materials. However, there are still challenges in the synthesis and characterization of these materials, and more research is needed to fully understand their properties and potential applications.

In this work a new zero-dimensional lead bromide hybrid material, $(C_5H_9N_3)_2PbBr_6$ was synthesized. The molecular structure, non-covalent bonds analysis (Hirshfeld surface analysis), and optical properties were characterized by UV-Visible and photoluminescence spectroscopies. The DFT calculation has been performed to determine the electronic structure of the compound, nature of semiconductor (direct or indirect) and to calculate the band gap energy.

2. Experimental and Computational Methods

2.1. Synthesis

Crystals of $(C_5H_9N_3)_2PbBr_6$ were synthesized by slow evaporation at room temperature method. The title compound was prepared by dissolving 2 mmol of 2,5-diaminopyridine and 1 mmol of lead (II) bromide ($PbBr_2$) in 10 ml of hydrobromic acid (HBr). Three weeks later, black single crystals suitable for structural determination were obtained.

2.2. X-ray Crystallography and Data Collection

A single black crystal of the title compound was selected, and X-ray intensity data were collected at 200 K on a Bruker dual- μ -source D8 Venture equipped with a Photon III detector single crystal diffractometer equipped with a HELIOS multilayer optics, using $AgK\alpha$ radiation ($\lambda = 0.56086 \text{ \AA}$). Intensity data were corrected for absorption effects by the Multi-scan method using the SADABS program [24]. The structure was solved and refined by full-matrix least squares based on F^2 using SHELXT [25] and SHELXL [25] respectively. All atoms were positioned from Fourier difference maps after looking at the bond length calculations. The atomic positions were refined with anisotropic displacement parameters. Hydrogen coordinates were idealized using appropriate HFIX instructions and included in subsequent least-squares refinement cycles in a riding motion approximation. Molecular graphics were prepared using Diamond 3 [26] and Mercury [27]. Crystal data and refinement parameters used for the intensity data collection are summarized in Table 1.

2.3. Physicochemical characterization

Thermogravimetric analysis (TG) and differential thermal analysis (DTA) were carried out in a stream of nitrogen using a "SETARM 92

Table 1

Crystal data and structure refinement parameters for $(C_5H_9N_3)_2PbBr_6$.

Empirical formula	$(C_5H_9N_3)_2PbBr_6$
Formula weight (g/mol)	454.48
Crystal system, space group	Triclinic, $P-1$
a (\AA)	7.5489 (3)
b (\AA)	7.9304 (3)
c (\AA)	9.6031 (4)
α ($^\circ$)	87.637 (1)
β ($^\circ$)	72.280 (1)
γ ($^\circ$)	76.771(1)
V (\AA^3)	532.84 (4)
Z	2
μ (mm^{-1})	10.35
D_x ($\text{g}\cdot\text{cm}^{-3}$)	2.833
$F(000)$	412.501
Crystal habit	Needle, Brown
$\theta_{\text{min}}/\theta_{\text{max}}$ (deg)	1.8/28
Measured reflections	38401
Independent reflections	5213
Observed refl. with $I > 2\sigma(I)$	4713
R_{int}	0.042
Data/restraints/parameters	5213 / 0/108
$R[F^2 > 2\sigma(F^2)]$	0.020
$wR(F^2)$	0.072
Goof = S	0.93
$\Delta\rho_{\text{max}} / \Delta\rho_{\text{min}}$ ($\text{e}\cdot\text{\AA}^{-3}$)	1.37 / -1.34
CCDC Number	2108060

16.18" instrument in the temperature range of 20 to 350°C with a ramp speed of $5^\circ\text{C}\cdot\text{min}^{-1}$. Room-temperature diffuse absorption and diffuse reflectance spectra of polycrystalline powder of $(C_5H_9N_3)_2PbBr_6$ were measured using a Shimadzu type 3101PC UV spectrophotometer in the wavelength range 200–800 nm.

Fluorescence measurements were carried out at room temperature using a Nanolog fluorescence spectrometer (Horiba Jobin-Yvon, New Jersey, USA) equipped with a UV 450W xenon-arc lamp. EEM data was generated by measuring the fluorescence emission from 300 to 750 nm on a thermally Peltier-cooled Si-based Front illuminated detector (1024×256 pixels) while exciting the powder at wavelengths ranging between 300 and 550 nm. The photoluminescence was recorded on powder (introduced into a perforated solid-sample holder) using a fiber optic bundle terminated by lenses, refocusing the exciting light onto an area of the material. The excitation and emission slits were set to a 2 and 4 nm band-pass, respectively and the integration time was set to 5 s for each wavelength. The Fluorescence™ software (Horiba Jobin-Yvon, New Jersey, USA) was used to collect the data and normalize the EEM data to the lamp intensity at each wavelength. The first and second-order Rayleigh bands were replaced with a curve fit using Labspec6 software (Horiba).

The electrical conductivity measurements are carried out on a sintered pellet. Studies of electrical conductivity are carried out after metallization by a layer of gold of the two parallel surfaces of this pellet. A Tegam3550 impedance analyzer is used for AC conductivity measurements which are performed in the temperature range of 443 K to 493 K. Complex impedance data, Z^* , can be represented by its real parts, Z' , and imaginary, Z'' , by the relation $Z^* = Z' - iZ''$.

2.4. Computational details

The electronic structure and the optical properties were carried out by using the density functional theory (DFT). The electron exchange-correlation functional (PBE) [28] and the projector augmented-wave (PAW) pseudo potential plane-wave method have been used by the means of the CASTEP code [29]. The crystal structure obtained from the X-ray single crystal refinement has been used as a starting model, and an energy cutoff of 600 eV was adopted with a regularly spaced mesh of $(2 \times 2 \times 2)$ points in the reciprocal unit cell. The atomic force, maximum displacement, and total energy convergence criteria were 0.05 eV \AA^{-1} ,

0.002 Å and 10^{-6} eV, respectively.

The Hirshfeld molecular surfaces were generated by Crystal Explorer program (version 17.5) [30,31]. The normalized contact distances, d_{norm} [32], based on Bondi van der Waals radii [33], were mapped into the Hirshfeld surface. In the color scale, negative values of d_{norm} are visualized by the red color indicating contacts shorter than the sum of van der Waals radii. The white areas signify intermolecular distances close to van der Waals contacts with d_{norm} equal to zero. Sequentially, contacts longer than the sum of van der Waals radii with positive d_{norm} values are colored in blue.

3. Results and discussion

3.1. Structure description

Single crystal X-ray diffraction data of $(\text{C}_5\text{H}_9\text{N}_3)_2\text{PbBr}_6$ was collected at 200K. The compound crystallizes in the triclinic system with space group *P*-1. The asymmetric unit of $(\text{C}_5\text{H}_9\text{N}_3)_2\text{PbBr}_6$ contains one cation $[\text{C}_5\text{H}_9\text{N}_3]^{2+}$ and half of the $[\text{PbBr}_6]^{4-}$ anion of the structure sits on a crystallographic inversion center (Fig. 1a).

The crystal packing of $(\text{C}_5\text{H}_9\text{N}_3)_2\text{PbBr}_6$ is depicted in Fig. 1b. The crystal structure shows an organic-inorganic layer arrangement parallel to the [010] direction. The organic layers can seem like zig-zag chains formed by the $[\text{C}_5\text{H}_9\text{N}_3]^{2+}$ molecules running on *a* direction and pillared along *b*. The inorganic $[\text{PbBr}_6]^{4-}$ octahedral units form a (4,4)-layer motif, with Pb(II)···Pb(II) distances of 7.5489(3) and 7.9304(3) Å along the *a* and *b* direction, respectively. The closest distance between adjacent Pb atoms along the *b* axis is approximately 7.930 Å, indicating that there is no electronic interaction between adjacent $[\text{PbBr}_6]^{4-}$ units. With Pb-Br bond lengths ranging from 2.9828(3) to 3.0228(3) Å, the Pb (II) ion has a slightly distorted octahedral configuration. The Br-Pb-Br angles vary from 85.564(8) to 94.436 (8)° for the cis and 180° for the trans arrangement (Table. S1). These values are comparable to those found in other halogenoplombates [34,35].

The stability of the structure is provided by the presence of N-H···Br (Fig. 2(a)) and C-H···Br (Fig. 2(b)) hydrogen bonds which ensure the linkage between $[\text{C}_5\text{H}_9\text{N}_3]^{2+}$ cations and $[\text{PbBr}_6]^{4-}$ anions. The possible hydrogen bonds present in the crystal structure are listed in Table 2. Although, $[\text{C}_5\text{H}_9\text{N}_3]^{2+}$ cations are arranged in a stacking manner due to offset π -stacking with alternative distances of 3.672 Å [Cg1···Cg1(-x,1-y,-z)] and 4.830 Å [Cg1···Cg1(1-x,1-y,-z)], respectively (Fig. 3).

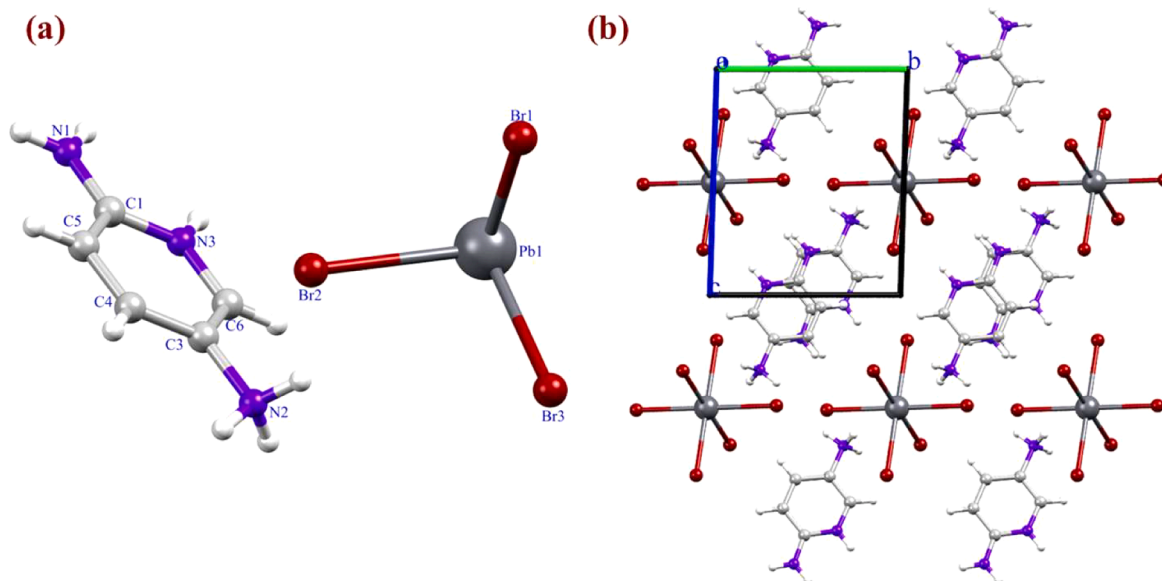


Fig. 1. (a) Asymmetric unit showing the atomic numbering scheme and (b) Packing diagram along the *b*-direction of $(\text{C}_5\text{H}_9\text{N}_3)_2\text{PbBr}_6$. (Dark grey: Lead, Red: Bromine; Light grey: carbon; Blue: Nitrogen and Pale green: Hydrogen).

3.2. Hirshfeld Surface Analysis for Structure of $(\text{C}_5\text{H}_9\text{N}_3)_2\text{PbBr}_6$.

The Hirshfeld surfaces and two-dimensional fingerprint plots were calculated to give an additional insight into the nature of intermolecular interactions in crystal packing [36–38]. The d_{norm} Hirshfeld surface, shape index and curvedness of $(\text{C}_5\text{H}_9\text{N}_3)_2\text{PbBr}_6$ are shown in Fig. 4 and the 2D fingerprint plots showing the percentage of area occupied by the most preponderant types of intermolecular interactions are depicted in Fig. 5. The intensive red spots on the surface colored according to d_{norm} correspond N/C-H···Br hydrogen bonds and N···Br halogen bonds with neighboring molecules. The small flat surface above the pyridine ring in the surface mapped with curvedness indicates the presence of stacking interactions in the structure. The presence of the adjacent red and blue triangles, obtained by using the shape index as a representation mode, also demonstrates the presence of stacking interactions [39–41]. The contribution of different types of interatomic contacts to the Hirshfeld surfaces of $(\text{C}_5\text{H}_9\text{N}_3)_2\text{PbBr}_6$ is shown in the fingerprint plots in Fig. 5. These interactions are ensured by 79.5% of hydrogen bonds (H···Br), 9.6% of H···H van der Waals interactions, 1.1 % of Y···X type (Br···Br, Br···N and Br···C), 3.4% of C···H/H···C contacts, 2.3 % of N···H/H···N and 4.1% of stacking interactions type (C···C and C···N/N···C). The percentages of contributions for a variety of contacts in the title compound are shown in (Fig. S2).

3.3. Powder X-Ray diffraction

The powder X-ray diffraction (PXRD) measurement was performed using a D8 ADVANCE BRUKER diffractometer using $\text{CuK}\alpha$ radiation. The measurements were carried out in the range 5 - 80° using a step size of $\Delta 2\theta = 0.015^\circ$ and a counting time of 2 sec/step. The Rietveld refinement was performed using the Fullprof software [42] and using the single crystal structure model as a starting set. The results of Rietveld refinement are shown in Fig. 6. The final agreement factors are: $R_p = 5.14$, $R_{wp} = 6.66$, $R_{exp} = 5.28$ and $\chi^2 = 1.59$.

3.4. Optical properties of $(\text{C}_5\text{H}_9\text{N}_3)_2\text{PbBr}_6$

The Fig. 7a represents the optical absorption spectrum of the compound $(\text{C}_5\text{H}_9\text{N}_3)_2\text{PbBr}_6$ recorded at room temperature and shows the presence of three peaks at 213, 299 and 335 nm. The excitation of an electron from the valence band to the conduction band explains the

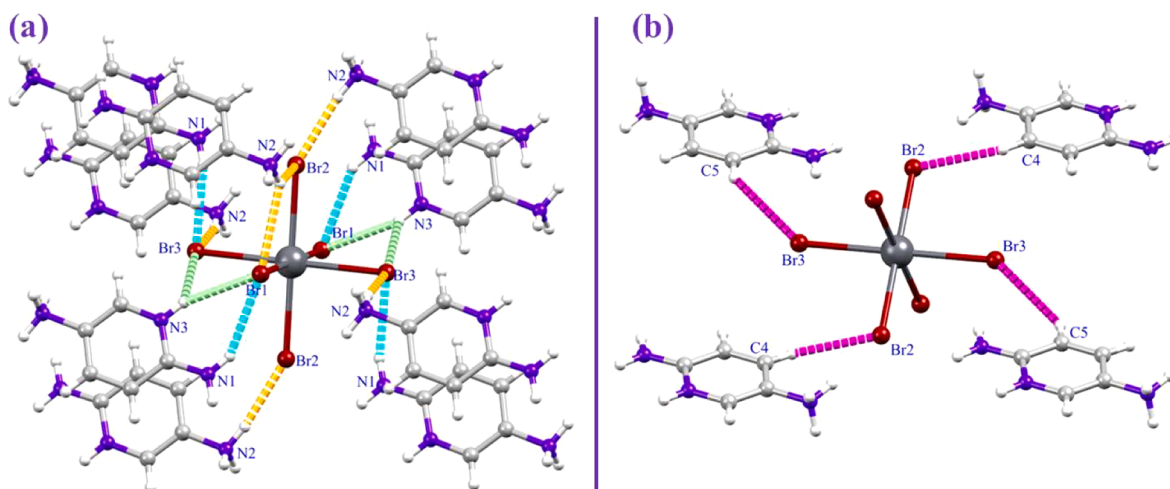


Fig. 2. (a) N-H...Br (N(ammonium)-H...Br orange dashed lines; N(amine)-H...Br cyan dashed lines and N(pyridine)-H...Br green dashed lines) and (b) C-H...Br hydrogen-bonds (pink dashed lines) in $(C_5H_9N_3)_2PbBr_6$.

Table 2
Hydrogen bond geometry (\AA , $^\circ$) in $(C_5H_9N_3)_2PbBr_6$.

D-H...A	D-H	H...A	D...A	D-H...A
N1-H1A...Br1 ⁱⁱⁱ	0.88	2.727(2)	3.491(2)	145.9
N1-H1B...Br3 ⁱⁱ	0.88	2.636(2)	3.448(2)	153.8
N2-H2A...Br3 ^v	0.91	2.428(19)	3.311(2)	163.1
N2-H2B...Br2 ^v	0.91	2.640(12)	3.329 (2)	169.86
N2-H2C...Br1 ⁱ	0.91	2.83(2)	3.399(2)	122.36
N2-H2C...Br2	0.91	2.642 (2)	3.284 (2)	128.30
N3-H3...Br1 ⁱⁱⁱ	0.88	2.788(2)	3.550(2)	145.7
N3-H3...Br1 ⁱⁱⁱ	0.88	2.836(2)	3.370(2)	120.6
C5-H5...Br3 ⁱⁱ	0.95	3.029 (2)	3.784(2)	137.46
C4-H4...Br2 ^{iv}	0.95	2.777(2)	3.566(2)	141.0

Symmetry codes:
ⁱ -x+1, -y, -z+1;
ⁱⁱ x, y+1, z-1;
ⁱⁱⁱ x, y, z-1;
^{iv} -x, -y+1, -z+1;
^v -x, -y, -z+1

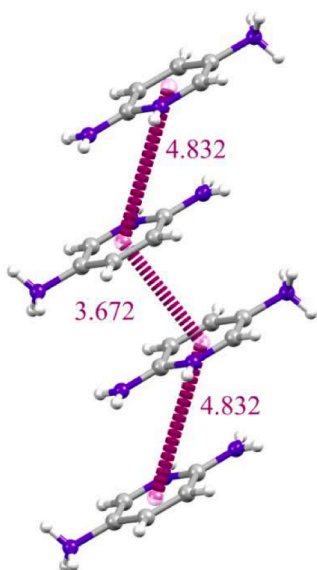


Fig. 3. Offset π -stacking between organic cations in $(C_5H_9N_3)_2PbBr_6$.

strong absorption in this spectrum (299 nm), as previously studied for the inorganic double-phase perovskite material $(CsPbBr_3-Cs_4PbBr_6)$ [43], indicating the band gap of this material. The other two bands (213 and 335 nm) can be attributed to $\pi \rightarrow \pi^*$ and $n \rightarrow \pi^*$ transitions in the conjugated rings of 2,5-diammoniumpyridine cations [44].

A diffuse reflectance measurement was carried out for the material to approximate its optical band gap by converting the reflectance spectrum into a Tauc plot, according to the Kubelka-Munk function:

$$\alpha h\nu = B(h\nu - E_g)^r \quad (1)$$

Where α is the absorption coefficient, E_g is the gap energy, B is a constant and r is a constant depending on the nature of the optical transition. As shown in Fig. 7a, the linear interpolation on the x axis of the graphical representation $(\alpha h\nu)^2$ (direct band gap) makes it possible to determine the energy of the optical band gap which is estimated to be 3.45 eV indicating a semi-conductive nature of the title material.

Room temperature fluorescence spectra were obtained to examine the luminescence characteristics of $(C_5H_9N_3)_2PbBr_6$. Excitation-emission matrices (EEM) were acquired prior to the common PL excitation and emission measurements to establish the best excitation and emission wavelengths. These are shown in Fig. 7b for the representative example $(C_5H_9N_3)_2PbBr_6$. Between 300-550 nm UV light excitation, the material exhibits a green emission band covering a large spectral region from 400 to 700 nm peaking at 592 nm. According to previous studies, we suppose that the main emissive species are $PbBr_4^{2-}$ anions. However, it may have resulted from exciton recombination within the inorganic substructures [45] or from local deformations in the band structure [46].

3.5. Thermal stability

The simultaneous (TG-DTA) curves of $(C_5H_9N_3)_2PbBr_6$ are presented in Fig. 8. During the heating cycle, no sequential phase transition was observed. This result suggests that the compound $(C_5H_9N_3)_2PbBr_6$ shows thermal stability up to 230°C and above this temperature continuous decomposition of the sample takes place. This decomposition process is accompanied by an endothermic peak on the DTA curve at 275°C followed by a total loss of the observed mass of the order of 20 %.

3.6. Electronic structure

The calculated band structure of $(C_5H_9N_3)_2PbBr_6$ is shown in Fig. 9. The maximum of the highest occupied valence bands and the minimum of lowest unoccupied conduction bands lie at the same point (Q-point)

Fig. 4. d_{norm} mapped on Hirshfeld surfaces for visualizing the intermolecular interactions, shape-index and curvedness of $(\text{C}_5\text{H}_9\text{N}_3)_2\text{PbBr}_6$.

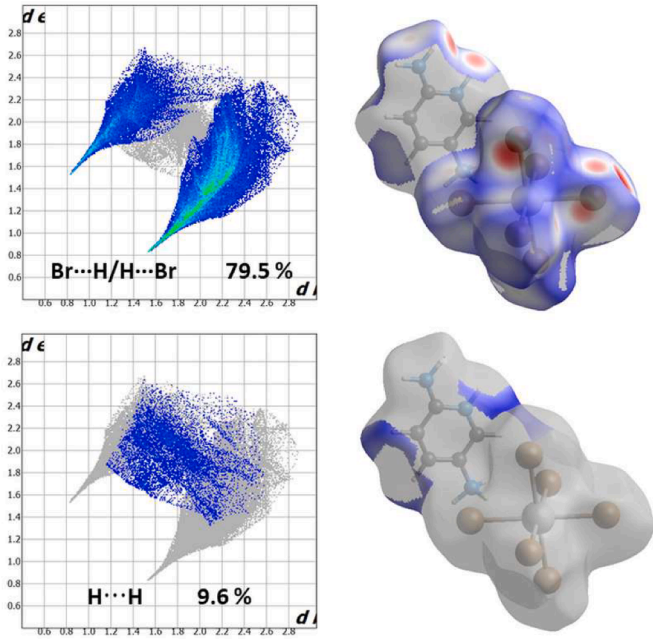
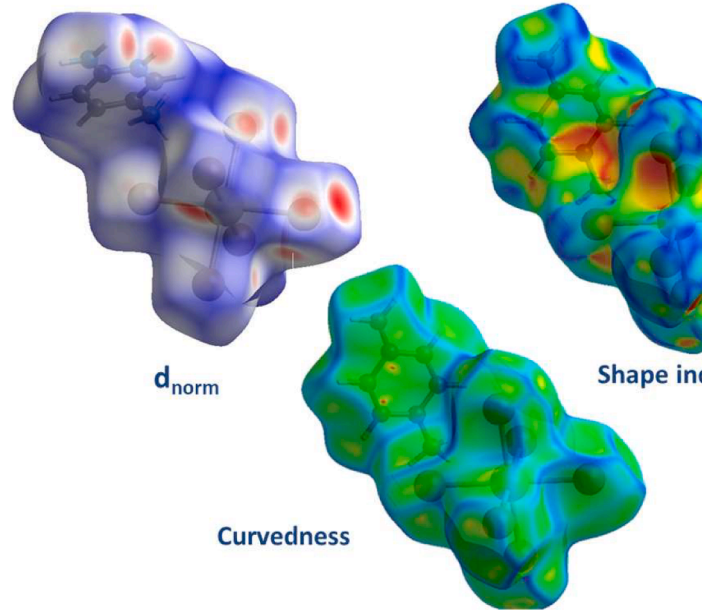


Fig. 5. Fingerprint plots of major contacts ($\text{Br}\cdots\text{H}/\text{H}\cdots\text{Br}$ and $\text{H}\cdots\text{H}$), and their corresponding HS in $(\text{C}_5\text{H}_9\text{N}_3)_2\text{PbBr}_6$.

(Fig. 9), thus the $(\text{C}_5\text{H}_9\text{N}_3)_2\text{PbBr}_6$ compound is a direct semiconductor. The band gap energy is about 2.97 eV (Fig. 9). This calculated energy value is lower than the experimental value determined from the UV-Visible absorption spectrum (Fig. 7a). This difference may be due to the self-interaction error of the XC functional [47–52].

The total and partial densities of states of $(\text{C}_5\text{H}_9\text{N}_3)_2\text{PbBr}_6$ are illustrated in Fig. 10. The Fermi level (indicated by a dotted line) is set to zero (E_F). Here, we have H: $1s^1$; C: $[\text{He}]2s^22p^2$; N: $[\text{He}]2s^22p^3$; Br^- : $[\text{Ar}]4s^23d^{10}4p^6$ and Pb^{2+} : $[\text{Xe}]6s^24f^{14}5d^{10}$ as valence electrons. The density of states representation is limited to -20; 8 eV window to better show the formation of bonds. Under -20 eV, there are two other bands formed Pb-6s at -136 eV and Pb-5d at -80 eV which we don't show for the good visualization of the other important band which are responsible in the

formation of the chemical band in the compound. The highest occupied crystal orbital is formed mostly of Br-4p and minority of C-2p and N-2p. The lowest unoccupied crystal orbital located above 2.97 eV are a mixture of C-2p and N-2p states.

3.7. Electrical properties

The complex shape of impedance is one of the important experimental techniques for analyzing the dynamics of ion mobility. The Cole-Cole analysis was performed in order to study the different contributions existing in the material. It can be noted in Fig. 11(a) that there is only one circular arc; this confirms the absence of contribution from the grain boundaries and the electrodes. With increasing temperature, the diameters of these arcs gradually decrease, suggesting a thermally activated process. Indeed, the increases in temperature are accompanied by an improvement in conductivity. In order to study the electrical behavior of the compound, we were led to choose an equivalent circuit most suited to our experimental data using the Z-View software. We have found that the most suitable circuit is composed of a single parallel cell formed by $(R_g \parallel \text{CPE}_g)$ for different temperatures.

The impedance of CPE is:

$$Z_{\text{CPE}} = \frac{1}{Q(j\omega)^\alpha} \quad (6)$$

Where Q corresponds to the value of capacitance and α stands for the parameter indicating the change of the compressed semicircle from an ideal semicircle.

The real and imaginary components of the whole impedance of this circuit were calculated according to the following expressions:

$$Z' = \frac{R_g + Q_g \omega^{\alpha_g} \cos\left(\frac{\alpha_g \pi}{2}\right) + R_g}{\left(1 + R_g Q_g \omega^{\alpha_g} \cos\left(\frac{\alpha_g \pi}{2}\right)\right)^2 + \left(R_g Q_g \omega^{\alpha_g} \sin\left(\frac{\alpha_g \pi}{2}\right)\right)^2} \quad (7)$$

$$-Z'' = \frac{R_g^2 Q_g \omega \cos\left(\frac{\alpha_g \pi}{2}\right)}{\left(1 + R_g Q_g \omega^{\alpha_g} \cos\left(\frac{\alpha_g \pi}{2}\right)\right)^2 + \left(R_g Q_g \omega^{\alpha_g} \sin\left(\frac{\alpha_g \pi}{2}\right)\right)^2} \quad (8)$$

Fig. 11(b) & (c) shows the variation of the real and imaginary parts of the impedance Z and Z'' with the angular frequency at different temperatures with their settings using Eq. (7) and Eq. (8).

It is observed that the value of Z' decreases with the increase of the temperature in the low frequency. At high frequencies, the spectrum

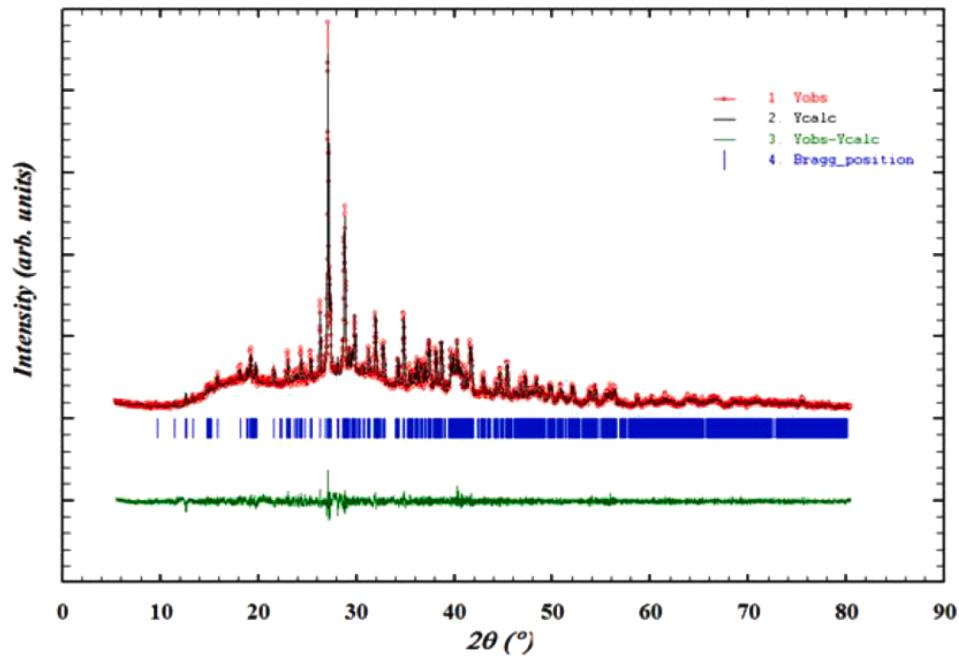


Fig. 6. The Rietveld refinement of the room temperature powder diffraction pattern of $(\text{C}_5\text{H}_9\text{N}_3)_2\text{PbBr}_6$.

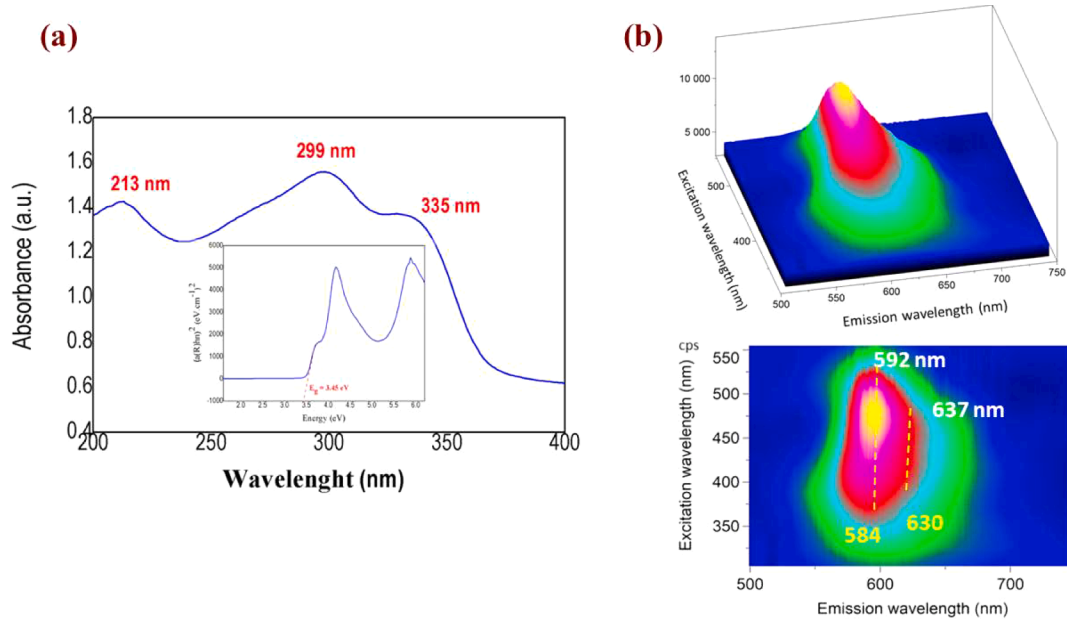


Fig. 7. (a) Absorption spectrum and diffuse reflectance spectrum in Kubelka-Munk unit, (b) Scanning the fluorescence intensity over a range of excitation and emission wavelengths (EEM) for $(\text{C}_5\text{H}_9\text{N}_3)_2\text{PbBr}_6$.

merged and became stable; this behavior can result from the release of a space charge following a decrease in the resistive behavior of the material [53]. It is observed from the variation of the imaginary part (Z'') as a function of the angular frequency that the amplitude of Z'' decreases with increasing temperature and that the peak frequency shifts towards higher values, which induces a thermally activated nature of the relaxation times. In all the temperatures the maximum of the peaks shifts towards the higher frequencies with the increase of temperature. This behavior points out the existence of a relaxation phenomenon [54,55].

The electrical conductivity (σ_{dc}) was calculated from the semi-circular parts (complex impedance adjustment) of Fig. 11(a) which is shown in Fig. 11(d).

This curve satisfies Arrhenius' law expressed in terms of [48].

$$\sigma_g T = \sigma_0 \exp\left(-\frac{E_a}{k_B T}\right) \quad (9)$$

This plot makes it possible to define the value of the activation energy which is equal to 1.18 eV.

In order to determine the conduction mechanism in the title compound, one can study the variation of the alternating conductivity as a function of the frequency (Fig. 11(e)). At low frequency, we observe the existence of a conductivity plateau independent of the frequency which increases with the temperature, it is the continuous conductivity obtained from complex impedance plots. At high frequency, the values of the alternating conductivity (σ_{ac}) approach because they are

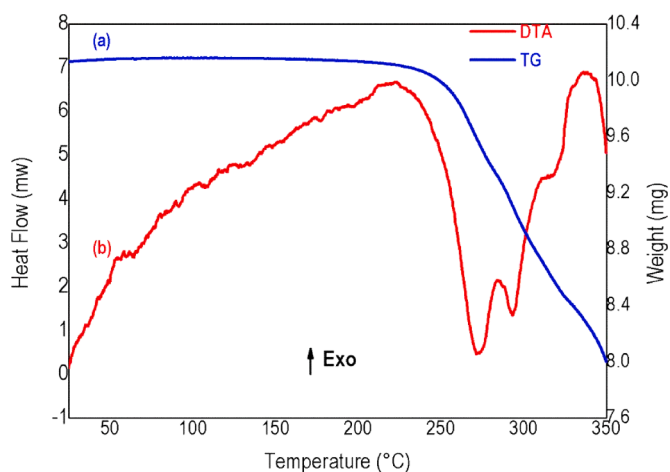


Fig. 8. TG-DTA curves for the decomposition of $(C_5H_9N_3)_2PbBr_6$, under flowing nitrogen ($5^\circ C/min$ from 20 to $350^\circ C$).

independent of the temperature. The conductivity increases with increasing temperature suggesting a superposition of different transport mechanisms which is found in semiconductor materials.

In order to get an idea about the relaxation procedure in $(C_5H_9N_3)_2PbBr_6$, detailed complex modulus spectra have been studied. The variation of imaginary part of electric modulus, M'' , with angular frequency at different temperatures is represented in Fig. 11(f). At a particular temperature, M'' acquires its maximum value which corresponds to the relaxation frequency. The peaks in M'' are found to shift toward the high frequency region with the increase in temperature, which can be explained by the hopping mechanism.

The asymmetrical nature of peaks in M'' indicates the non-Debye response of the sample [56]. The imaginary part of $M''(\omega)$ was approximated as follow [57]:

$$M'' = \frac{M''_{max}}{(1 - \beta) + \left(\frac{\beta}{1 + \beta}\right) \left(\beta \left(\frac{\omega_{max}}{\omega}\right) + \left(\frac{\omega}{\omega_{max}}\right)\right)^\beta} \quad (10)$$

Where ω_{max} express the frequency corresponding to the maximum modulus M'' ; β ($0 \leq \beta \leq 1$, $\beta = 1$ for Debye relaxation) reflects the

importance of coupling between mobile ions in the conduction process.

The activation energy of the relaxation processes can be calculated from the slope of the curve of $\ln(\omega_{max})$ as a function of $1000/T$. This curve Fig. 11(g) exhibits Arrhenius-type behavior defined by the law given by the following equation:

$$\omega_m = \omega_0 \exp\left(-\frac{E_m}{k_B T}\right) \quad (11)$$

Where E_m is the activation energy for the relaxation time and ω_0 is the pre-exponential factor.

From the linear fit, the calculated activation energy is equal to 1.14 eV.

The frequencies dependence of variation of normalized parameters Z''/Z''_{max} and M''/M''_{max} is shown in Fig. 11(h) in order to determine if the conduction is localized or non-localized. In the case where Z'' and M'' peaks are separated in material exist localized relaxation otherwise when the peaks in these two curves are overlapping in material exist non-localized or a long-range relaxation [58]. It is noted that there is an offset between Z'' and M'' indicating the short-range conduction of charge carriers located in this material.

4. Conclusion

To summarize, we have successfully synthesized a novel single-crystalline assembly of metal halide clusters $(C_5H_9N_3)_2PbBr_6$, where the $PbBr_6$ isolated octahedral clusters construct a 0D perovskite-like anionic framework. This material crystallizes in the $P-1$ triclinic space group. The combinations of hydrogen bonding, and π -stacking interactions are described. Hirshfeld surface analysis implies that the hydrogen bonds $Br \cdots H$ and $H \cdots H$ are the driving forces of molecular arrangement. Optical absorption revealed that the band gap of this compound is 3.45 eV showing semiconductor nature. Two green bands emission were obtained in this material. The analysis of the electrical conductivity shows that the most adequate equivalent circuit in this material is represented by a single parallel cell formed by $(R_g \parallel CPE_g)$, the value of the activation energy is 1.18 eV. The activation energy calculated for the relaxation time is equal to 1.14 eV. There is a shift between Z'' and M'' which proves the short distance conduction of the charge carriers located in this material. The calculated band gap value is smaller than experimental value determined from the optical spectrum, which

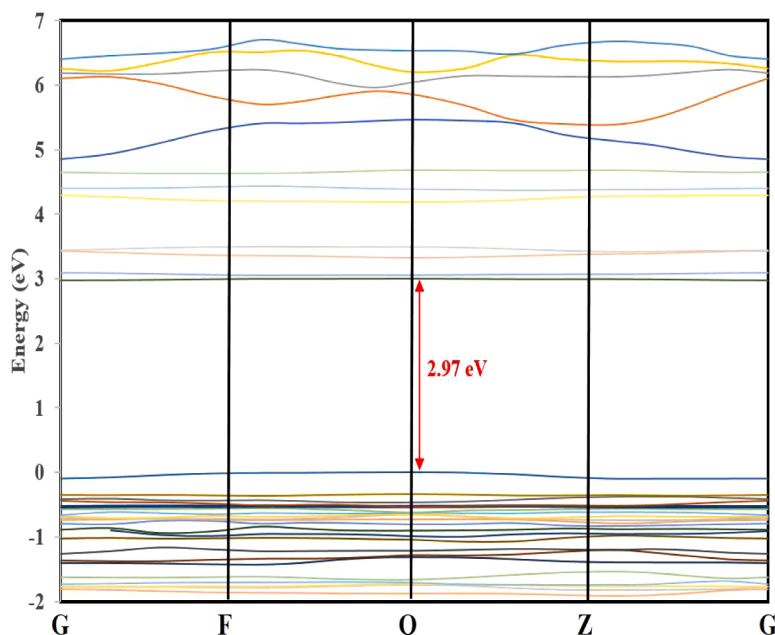


Fig. 9. Electronic Band structure of $(C_5H_9N_3)_2PbBr_6$.

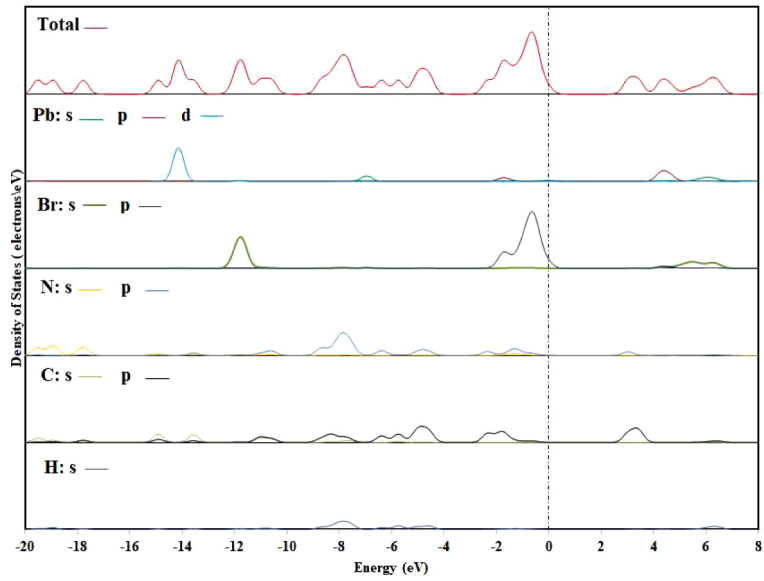


Fig. 10. Total and partial density of states of $(C_5H_9N_3)_2PbBr_6$.

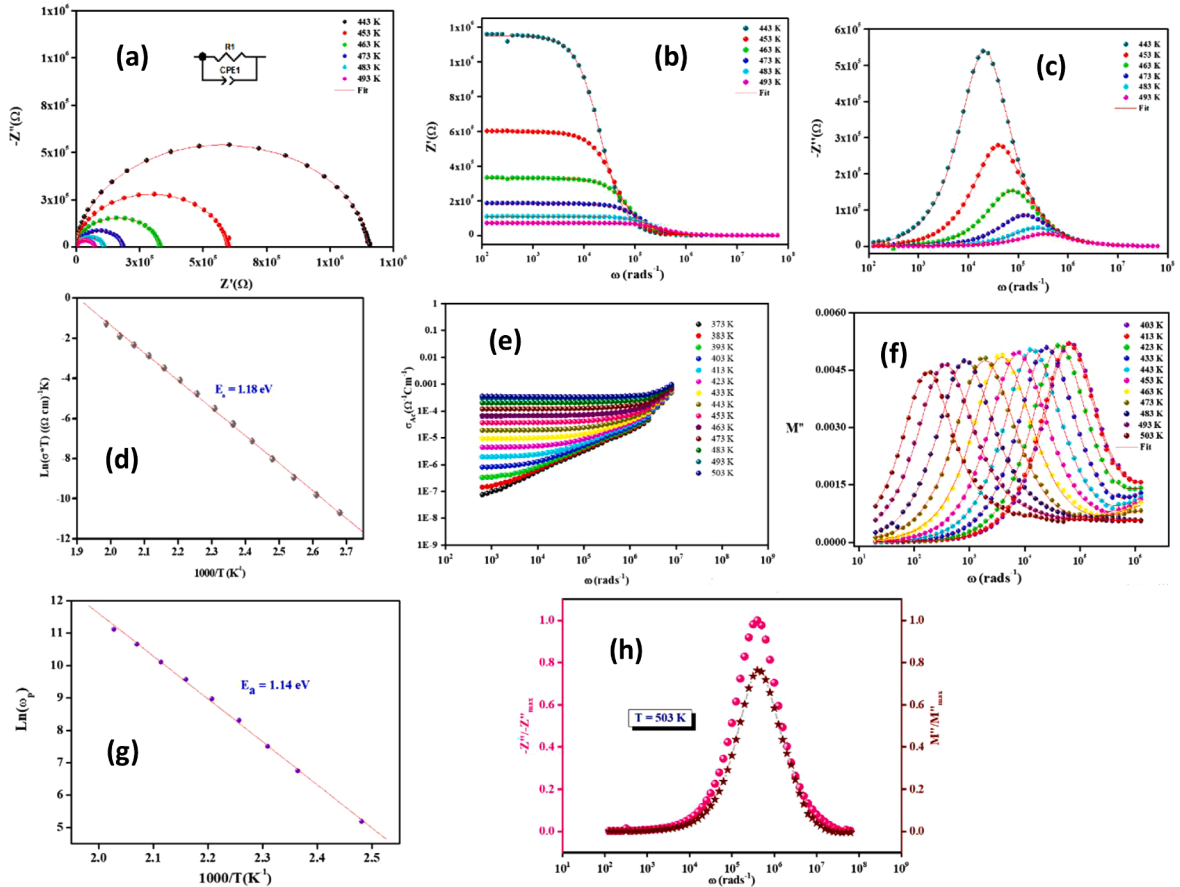


Fig. 11. (a) Complex impedance plot ($-Z''$ vs Z') for $(C_5H_9N_3)_2PbBr_6$ pellets. The solid line (red) passing through the data points represents the fitted data using the equivalent software. (b) Variation of real Z' and (c) Imaginary Z'' part of impedance with frequency at different temperatures. (d) Arrhenius representation of the dc conductivity in air. (e) Variation of ac conductivity (σ_{ac}) with frequency at different temperatures. (f) Variation of imaginary part of electric modulus (M'') with frequency at different temperatures. (g) Variation of $\ln(\sigma_{max})$ as a function of $1000/T$ at different temperatures. (h) Variation of Z''/Z''_{max} and M''/M''_{max} as a function of frequency at 503 K.

may be due to the self-interaction error of the XC functional. Our work brings a new emissive member to lead bromide zero-dimensional family and could be interesting for electronic and photonic applications such as

LED and optical sensors.

References

- [1] S. Sandrez, Z. Molenda, C. Guyot, O. Renault, J.P. Barnes, L. Hirsch, T. Maindron, G. Wantz, Halide Perovskite Precursors Dope PEDOT: PSS, *Advanced Electronic Materials* 7 (2021), 2100394.
- [2] R. Li, C. Yi, R. Ge, W. Zou, L. Cheng, N. Wang, J. Wang, W. Huang, Room-temperature electroluminescence from two-dimensional lead halide perovskites, *Applied Physics Letters* 109 (2016), 151101.
- [3] V.S. Chirvony, S. González-Carrero, I. Suarez, R.E. Galian, M. Sessolo, H.J. Bolink, J.P. Martínez-Pastor, J. Perez-Prieto, Delayed luminescence in lead halide perovskite nanocrystals, *The Journal of Physical Chemistry C* 121 (2017) 13381–13390.
- [4] A. Kojima, K. Teshima, Y. Shirai, T. Miyasaka, Organometal halide perovskites as visible-light sensitizers for photovoltaic cells, *Journal of the American Chemical Society* 131 (2009) 6050–6051.
- [5] M.D. Perez, J. Plá, Emergent materials and concepts for solar cell applications. *Sustainable Material Solutions for Solar Energy Technologies*, Elsevier, 2021, pp. 37–70.
- [6] T. Kataoka, T. Kondo, R. Ito, S. Sasaki, K. Uchida, N. Miura, Magneto-optical study on excitonic spectra in (C₆H₁₃NH₃)₂PbI₄, *Physical Review B* 47 (1993) 2010.
- [7] D.B. Mitzi, K. Chondroudis, C.R. Kagan, Organic-inorganic electronics, *IBM Journal of research and development* 45 (2001) 29–45.
- [8] D.B. Mitzi, Synthesis, crystal structure, and optical and thermal properties of (C₄H₉NH₃)₂M₂I₄ (M = Ge, Sn, Pb), *Chemistry of materials* 8 (1996) 791–800.
- [9] J. Chen, Y. Wang, Personalized dynamic transport of magnetic nanorobots inside the brain vasculature, *Nanotechnology* 31 (2020), 495706.
- [10] J. Cao, J. Jiang, N. Li, Y. Dong, Y. Jia, S. Tao, N. Zhao, Alkali-cation-enhanced benzylammonium passivation for efficient and stable perovskite solar cells fabricated through sequential deposition, *Journal of Materials Chemistry A* 8 (2020) 19357–19366.
- [11] C.J. Dahlman, R.A. DeCrescent, N.R. Venkatesan, R.M. Kennard, G. Wu, M. A. Everest, J.A. Schuller, M.L. Chabinyc, Controlling Solvate Intermediate Growth for Phase-Pure Organic Lead Iodide Ruddlesden–Popper (C₄H₉NH₃)₂(CH₃NH₃)_{n-1}Pb_nI_{3n+1} Perovskite Thin Films, *Chemistry of Materials* 31 (2019) 5832–5844.
- [12] H. Min, D.Y. Lee, J. Kim, G. Kim, K.S. Lee, J. Kim, M.J. Paik, Y.K. Kim, K.S. Kim, M. G. Kim, Perovskite solar cells with atomically coherent interlayers on SnO₂ electrodes, *Nature* 598 (2021) 444–450.
- [13] L. Etgar, The merit of perovskite's dimensionality; can this replace the 3D halide perovskite? *Energy & Environmental Science* 11 (2018) 234–242.
- [14] G. Wu, C. Zhou, W. Ming, D. Han, S. Chen, D. Yang, T. Besara, J. Neu, T. Siegrist, M.-H. Du, A one-dimensional organic lead chloride hybrid with excitation-dependent broadband emissions, *ACS Energy Letters* 3 (2018) 1443–1449.
- [15] J. Zhou, M. Li, L. Ning, R. Zhang, M.S. Molokeev, J. Zhao, S. Yang, K. Han, Z. Xia, Broad-band emission in a zero-dimensional hybrid organic [PbBr₆] trimer with intrinsic vacancies, *The Journal of physical chemistry letters* 10 (2019) 1337–1341.
- [16] Y. Tian, Q. Wei, H. Peng, Z. Yu, S. Yao, B. Ke, Q. Li, B. Zou, A Zero-Dimensional Organic Lead Bromide of (TPA)₂PbBr₄ Single Crystal with Bright Blue Emission, *Nanomaterials* 12 (2022) 2222.
- [17] M.I. Saidaminov, J. Almutlaq, S. Sarmah, I. Dursun, A.A. Zhumekenov, R. Begum, J. Pan, N. Cho, O.F. Mohammed, O.M. Bakr, Pure Cs₄PbBr₆: highly luminescent zero-dimensional perovskite solids, *ACS Energy Letters* 1 (2016) 840–845.
- [18] Y. Wei, T. Ma, J. Chen, M. Zhao, H. Zeng, Metal halide perovskites for optical parametric modulation, *The Journal of Physical Chemistry Letters* 12 (2021) 3090–3098.
- [19] D. Cortecchia, J. Yin, A. Petrozza, C. Soci, White light emission in low-dimensional perovskites, *Journal of Materials Chemistry C* 7 (2019) 4956–4969.
- [20] D. Han, H. Shi, W. Ming, C. Zhou, B. Ma, B. Saparov, Y.-Z. Ma, S. Chen, M.-H. Du, Unraveling luminescence mechanisms in zero-dimensional halide perovskites, *Journal of Materials Chemistry C* 6 (2018) 6398–6405.
- [21] D. Cortecchia, J. Yin, A. Bruno, S.-Z.A. Lo, G.G. Gurzadyan, S. Mhaisalkar, J.-L. Brédas, C. Soci, Polaron self-localization in white-light emitting hybrid perovskites, *Journal of Materials Chemistry C* 5 (2017) 2771–2780.
- [22] C. Zhou, H. Lin, Q. He, L. Xu, M. Worku, M. Chaaban, S. Lee, X. Shi, M.-H. Du, B. Ma, Low dimensional metal halide perovskites and hybrids, *Materials Science and Engineering: R: Reports* 137 (2019) 38–65.
- [23] V. Morad, Y. Shynkarenko, S. Yakunin, A. Brumberg, R.D. Schaller, M. V. Kovalenko, Disphenoidal zero-dimensional lead, tin, and germanium halides: Highly emissive singlet and triplet self-trapped excitons and X-ray scintillation, *Journal of the American Chemical Society* 141 (2019) 9764–9768.
- [24] G. Sheldrick, SADABS Bruker Axs Inc (2007).
- [25] G.M. Sheldrick, Crystal structure refinement with SHELXL, *Acta Crystallographica Section C: Structural Chemistry* 71 (2015) 3–8.
- [26] K. Brandenburg, Diamond version 2.0 impact GbR, Bonn, Germany, 1998.
- [27] J. Chambers, F. Migliorini, MERCURY-a new software package for orbital integrations, AAS/Division for Planetary Sciences Meeting Abstracts# 29, 1997, p. 27.06.
- [28] J.P. Perdew, K. Burke, M. Ernzerhof, Generalized gradient approximation made simple, *Physical review letters* 77 (1996) 3865.
- [29] M. Segall, P.J. Lindan, M.a. Probert, C.J. Pickard, P.J. Hasnip, S. Clark, M. Payne, First-principles simulation: ideas, illustrations and the CASTEP code, *Journal of physics: condensed matter* 14 (2002) 2717.
- [30] C.F. Mackenzie, P.R. Spackman, D. Jayatilaka, M.A. Spackman, CrystalExplorer model energies and energy frameworks: extension to metal coordination compounds, organic salts, solvates and open-shell systems, *IUCrJ* 4 (2017) 575–587.
- [31] M.A. Spackman, D. Jayatilaka, Hirshfeld surface analysis, *CrystEngComm* 11 (2009) 19–32.
- [32] J.J. McKinnon, D. Jayatilaka, M.A. Spackman, Towards quantitative analysis of intermolecular interactions with Hirshfeld surfaces, *Chemical Communications* (2007) 3814–3816.
- [33] A. Bondi, Van der Waals volumes and radii of metals in covalent compounds, *The Journal of Physical Chemistry* 70 (1966) 3006–3007.
- [34] B.A. Rosales, M.P. Hanrahan, B.W. Boote, A.J. Rossini, E.A. Smith, J. Vela, Lead halide perovskites: Challenges and opportunities in advanced synthesis and spectroscopy, *ACS Energy Letters* 2 (2017) 906–914.
- [35] H. Xu, J. Sun, A. Qin, J. Hua, Z. Li, Y. Dong, H. Xu, W. Yuan, Y. Ma, M. Wang, Functional perovskite hybrid of polyacetylene ammonium and lead bromide: synthesis, light emission, and fluorescence imagining, *The Journal of Physical Chemistry B* 110 (2006) 21701–21709.
- [36] A.-A.B. OmarAli, R.K. Ahmed, A.J.M. Al-Karawi, S. Marah, S. Kansiz, Y. Sert, M. I. Jaafar, N. Dege, E.B. Poyraz, A.M. Ahmed, Designing of two new cadmium (II) complexes as bio-active materials: Synthesis, X-ray crystal structures, spectroscopic, DFT, and molecular docking studies, *Journal of Molecular Structure* 1290 (2023), 135974.
- [37] S. Adhikari, A.H. Sheikh, S. Kansiz, N. Dege, N. Baildya, G. Mahmoudi, N. A. Choudhury, R.J. Butcher, W. Kaminsky, S. Talledo, Supramolecular Co (II) complexes based on dithiolate and dicarboxylate ligands: Crystal structures, theoretical studies, magnetic properties, and catalytic activity studies in photocatalytic hydrogen evolution, *Journal of Molecular Structure* 1285 (2023), 135481.
- [38] E. Alaman, A. Agar, M. Tahir, M. Ashfaq, E. Poyraz, N. Dege, Synthesis, Structural, Spectroscopic, Hirshfeld Surface Analysis and Computational Study of Copper Complex Containing Salicylaldehyde Ligands, *Journal of Structural Chemistry* 64 (2023) 1314–1328.
- [39] S. Baaziz, E. Poyraz, R. Benali-Cherif, W. Falek, B. Hannachi, N. Dege, E. Bendeif, N. Benali-Cherif, Crystal Structure, Hirshfeld Surface Analysis and IR Analysis of 2-Amino-1, 9-Dihydro-6H-Purin-6-One-Selenate-Water, *Journal of Structural Chemistry* 64 (2023) 1350–1359.
- [40] R. Saddik, S.A. Brandán, S. Mortada, C. Baydere, O. Roby, N. Dege, S. Tighadouini, M. Tahiri, M.A. Faouzi, K. Karrouchi, Synthesis, crystal structure, Hirshfeld surface analysis, DFT and antihyperglycemic activity of 9-allyl-2, 3, 9, 10a-tetrahydro-benzo [b] cyclopenta [e][1, 4] diazepin-10 (1H)-one, *Journal of Molecular Structure* 1283 (2023), 135283.
- [41] E. Acar, S. Kansiz, N. Dege, Synthesis, Crystal Structure and Hirshfeld Surface Analysis of (E)-2-(4-Methylbenzylidene)-N-Phenylhydrazine-1-Carbothioamide, *Journal of Structural Chemistry* 64 (2023) 974–983.
- [42] H. Rietveld, Line profiles of neutron powder-diffraction peaks for structure refinement, *Acta Crystallographica* 22 (1967) 151–152.

- [43] Z. Bao, H.-D. Chiu, W. Wang, Q. Su, T. Yamada, Y.-C. Chang, S. Chen, Y. Kanemitsu, R.-J. Chung, R.-S. Liu, Highly luminescent CsPbBr₃@ Cs₄PbBr₆ nanocrystals and their application in electroluminescent emitters, *The Journal of Physical Chemistry Letters* 11 (2020) 10196–10202.
- [44] M. Pagliai, G. Mancini, I. Carmimeo, N. De Mitri, V. Barone, Electronic absorption spectra of pyridine and nicotine in aqueous solution with a combined molecular dynamics and polarizable QM/MM approach, *Journal of Computational Chemistry* 38 (2017) 319–335.
- [45] A. Yangui, R. Roccanova, Y. Wu, M.-H. Du, B. Saparov, Highly efficient broad-band luminescence involving organic and inorganic molecules in a zero-dimensional hybrid lead chloride, *The Journal of Physical Chemistry C* 123 (2019) 22470–22477.
- [46] P. Kumar, Q. Shi, K.J. Karki, Enhanced radiative recombination of excitons and free charges due to local deformations in the band structure of MAPbBr₃ perovskite crystals, *The Journal of Physical Chemistry C* 123 (2019) 13444–13450.
- [47] J. Ruiz-Fuertes, S. López-Moreno, J. López-Solano, D. Errandonea, A. Segura, R. Lacomba-Perales, A. Muñoz, S. Radescu, P. Rodríguez-Hernández, M. Gospodinov, Pressure effects on the electronic and optical properties of A WO₄ wolframites (A= Cd, Mg, Mn, and Zn): The distinctive behavior of multiferroic MnWO₄, *Physical Review B* 86 (2012), 125202.
- [48] V. Panchal, D. Errandonea, A. Segura, P. Rodríguez-Hernández, A. Muñoz, S. Lopez-Moreno, M. Bettinelli, The electronic structure of zircon-type orthovanadates: Effects of high-pressure and cation substitution, *Journal of Applied Physics* 110 (2011), 043723.
- [49] M.H. Lakhdar, Y.B. Smida, M. Amlouk, Synthesis, optical characterization and DFT calculations of electronic structure of Sb₂O₃ films obtained by thermal oxidation of Sb₂S₃, *Journal of Alloys and Compounds* 681 (2016) 197–204.
- [50] M.P. Motaung, J.O. Adeyemi, Y.B. Smida, H. Ferjani, M.M. Kabanda, D. C. Onwudiwe, E. Hosten, Synthesis, structural, and DFT studies of Cu (II) dithiocarbamate complexes, *Journal of Molecular Structure* 1271 (2023), 133988.
- [51] H.F. Youssef Ben Smida, Abdelwaheb Boukhachem, Damian C. Onwudiwe, Nuha Y. Elamin, Ahmed Hichem Hamzaoui, Ab initio study of the optoelectronic properties of α-Ba₂SnS₄, *Materials Science in Semiconductor Processing* (2022).
- [52] H. Ferjani, Y. Ben Smida, D.C. Onwudiwe, N.Y. Elamin, S. Ezzine, N.S. Almotlaq, An Experimental and Theoretical Study of the Optical Properties of (C₂H₇N₄O)₂BiCl₅ for an Optoelectronic Application, *Inorganics* 10 (2022) 48.
- [53] J. Suchanicz, The low-frequency dielectric relaxation Na_{0.5}Bi_{0.5}TiO₃ ceramics, *Materials Science and Engineering: B* 55 (1998) 114–118.
- [54] Y. Ben Taher, A. Oueslati, N. Maaloul, K. Khirouni, M. Gargouri, Conductivity study and correlated barrier hopping (CBH) conduction mechanism in diphosphate compound, *Applied Physics A* 120 (2015) 1537–1543.
- [55] M. Shah, M. Nadeem, M. Idrees, M. Atif, M. Akhtar, Change of conduction mechanism in the impedance of grain boundaries in Pr_{0.4}Ca_{0.6}MnO₃, *Journal of magnetism and magnetic materials* 332 (2013) 61–66.
- [56] P. Khatri, B. Behera, R. Choudhary, Structural and electrical properties of Sr₃V₂O₈ ceramics, *physica status solidi (b)* 246 (2009) 1118–1123.
- [57] R. Bergman, General susceptibility functions for relaxations in disordered systems, *Journal of Applied Physics* 88 (2000) 1356–1365.
- [58] R. Gerhardt, Impedance and dielectric spectroscopy revisited: distinguishing localized relaxation from long-range conductivity, *Journal of Physics and Chemistry of Solids* 55 (1994) 1491–1506.